

Retrieving sea surface salinity with multiangular L-band brightness temperatures: Improvement by spatiotemporal averaging

A. Camps, M. Vall-llossera, L. Batres, F. Torres, N. Duffo, and I. Corbella

Department of Signal Theory and Communications, Universitat Politècnica de Catalunya, Barcelona, Spain

Received 4 February 2004; revised 30 August 2004; accepted 3 January 2005; published 31 March 2005.

[1] The Soil Moisture and Ocean Salinity (SMOS) mission was selected in May 1999 by the European Space Agency to provide global and frequent soil moisture and sea surface salinity maps. SMOS' single payload is Microwave Imaging Radiometer by Aperture Synthesis (MIRAS), an L band two-dimensional aperture synthesis interferometric radiometer with multiangular observation capabilities. Most geophysical parameter retrieval errors studies have assumed the independence of measurements both in time and space so that the standard deviation of the retrieval errors decreases with the inverse of square root of the number of measurements being averaged. This assumption is especially critical in the case of sea surface salinity (SSS), where spatiotemporal averaging is required to achieve the ultimate goal of 0.1 psu error. This work presents a detailed study of the SSS error reduction by spatiotemporal averaging, using the SMOS end-to-end performance simulator (SEPS), including thermal noise, all instrumental error sources, current error correction and image reconstruction algorithms, and correction of atmospheric and sky noises. The most important error sources are the biases that appear in the brightness temperature images. Three different sources of biases have been identified: errors in the noise injection radiometers, Sun contributions to the antenna temperature, and imaging under aliasing conditions. A calibration technique has been devised to correct these biases prior to the SSS retrieval at each satellite overpass. Simulation results show a retrieved salinity error of 0.2 psu in warm open ocean, and up to 0.7 psu at high latitudes and near the coast, where the external calibration method presents more difficulties.

Citation: Camps, A., M. Vall-llossera, L. Batres, F. Torres, N. Duffo, and I. Corbella (2005), Retrieving sea surface salinity with multiangular L-band brightness temperatures: Improvement by spatiotemporal averaging, *Radio Sci.*, 40, RS2003, doi:10.1029/2004RS003040.

1. Introduction

[2] The scientific objectives of the SMOS mission are listed in Table 1. These objectives can be achieved by microwave radiometry at L band. However, real aperture radiometers require antennas of several meters in diameter to achieve the required spatial resolution from space. To overcome this problem, SMOS exploits for the first time in Earth observation from space, the 2-D aperture synthesis interferometric radiometry concept used for decades in radioastronomy [Thompson *et al.*, 1986].

[3] The data processing involved to obtain a brightness temperature image is complex and includes detailed instrument modeling of receivers [Torres *et al.*, 1997] and antennas [Camps *et al.*, 1997b, 1998b], error correction by distributed noise injection [Torres *et al.*, 1996; Corbella *et al.*, 1998], and image reconstruction algorithms [Camps *et al.*, 1998a, 2004b]. In the ideal case of identical receivers and antenna voltage patterns, and negligible spatial decorrelation effects, the relationship between the samples of the so-called "visibility function" (obtained from the cross-correlation products of the signals collected by each pair of receiving elements) and the brightness temperature images (T_x and T_y in the antenna reference frame) expressed in the direction cosines domain $(\xi, \eta) = (\sin \theta \cos \varphi, \sin \theta \sin \varphi)$ reduces

to a Fourier transform. The samples of the visibility function are measured by the interferometric radiometer at a set of spatial wave numbers (u, v) determined by the spacing between the pair of antennas normalized to the wavelength: $(u, v) = (x_2 - x_1, y_2 - y_1)/\lambda$.

[4] In SMOS the antennas are distributed along three arms 120° apart and are spaced $d = 0.875$ wavelengths (Figure 1a). However, the Nyquist criterion for hexagonal sampling requires that the antenna separation be $d = 1/\sqrt{3}$ wavelengths to avoid aliasing in the unit circle ($\xi^2 + \eta^2 = 1$) [Camps *et al.*, 1997a]. Therefore the reconstructed 2-D brightness temperature images suffer from aliasing and replicas of the Earth image (“aliases”) overlap with the Earth image in the fundamental period (Figure 1b), which defines the alias-free field of view (AF-FOV). Each pixel in the AF-FOV is seen at a different incidence angle, radiometric sensitivity, and spatial resolution (Figure 1c). As the satellite moves, the projection of the AF-FOV in cross-track/along-track Earth coordinates is displaced from snapshot to snapshot, and pixels are then seen in different positions in the AF-FOV at different incidence angles. Figure 1b represents the equi-incidence angle contours in the AF-FOV as shown in the work of Camps *et al.* [2003a, 2003b].

[5] As in the work of Camps *et al.* [2003a], the SSS retrieval algorithm is stated as a minimization problem of the mean squared error between the measured first Stokes parameter (computed as the sum of the brightness temperature images at both polarizations measured in the antenna reference frame and the one modeled using estimated parameters for all pixels within the swath width (Figure 2). (Existing measurements and theoretical predictions show that the third Stokes parameters at L and is negligible.)

$$\varepsilon = \frac{1}{N_{\text{observations}}} \sum_{n=1}^{N_{\text{observations}}} \left[\left(I_n^{\text{model}}(\theta_n, \hat{U}_{10}, \hat{S}\hat{S}\hat{T}, \hat{S}\hat{S}\hat{S}) - I_n^{\text{data}} \right)^2 \frac{t(\theta, \phi)}{\cos \theta} \right]. \quad (1)$$

The parameters to be recovered are the sea surface salinity (SSS), the sea surface temperature (SST), and the effective 10 m height wind speed (\hat{U}_{10}), which accounts for sea state effects (wind-induced waves, swell, etc.) and not just the waves induced by the wind. This procedure has shown a better performance than having SST and U_{10} constant with a value equal to the ancillary data provided by other instruments [Gabarró *et al.*, 2003]. Since I_n^{data} are independent, the covariance matrix is diagonal, and only the terms $t(\theta, \phi)$ (average normalized antenna radiation pattern of all receiving elements) and $\cos \theta = \sqrt{1 - \xi^2 - \eta^2}$ (obliquity factor) are needed to weight the radiometric measurements according to the noise in each

Table 1. Main Scientific Objectives of the SMOS Mission

Scientific Objectives	Requirements
	<i>Ocean</i>
Global sea surface salinity maps	0.1 psu every 10–30 days 200 km spatial resolution
	<i>Land</i>
Global soil moisture Vegetation water content maps Cryosphere (experimental)	0.035 m ³ /m ³ every 3 days 0.2 kg/m ² 60 km spatial resolution improved snow mantle monitoring and multilayer ice structure.

pixel of the 2-D brightness temperature image. The number $N_{\text{observations}}$ is the number of measurements acquired of the same location (pixel) in a satellite overpass, and it is determined by the satellite’s ground speed and the length of the dwell line (maximum distance in the AF-FOV in the along-track direction). Owing to the instrument’s limited angular resolution, Earth “aliases” enter in the nominal AF-FOV. (MIRAS’ angular resolution is 2.25° if the visibility samples are tapered with a Blackman window prior to the image reconstruction.) Contribution from Earth aliases is negligible if a guard region of width $\sim 1.5^\circ$ (or $\Delta\xi = 0.026$) is kept, which also reduces slightly the maximum swath width. Figure 2 presents the pixels that are imaged for the first time in an overpass. As the distance to the ground track (abscissa in Figure 1c) increases, the number of observations decreases (length of dwell line shortens) and measurements become noisier (Figure 1c) due to the antenna pattern and obliquity factor compensation in the image reconstruction process, which increases the magnitude of the retrieved parameter errors. This effect is seen more clearly in the series of simulated brightness temperature observations over the Earth for different cross-track distances to the satellite’s ground track (Figures 3a–3f). The number of observations increases as the dwell line approaches the ground track, reaching a maximum around the cross-track position 250 km and then slightly decreases again. In addition, each observation is acquired at a different incidence angle, and pixels in dwell lines close to the ground track are imaged twice at the same incidence angle in the fore and aft directions (Figure 3f).

[6] The minimization of equation (1) is performed using a recurrent Levenberg-Marquardt least squares fit [Press *et al.*, 1992]. Without loss of generality, the first guess values are assumed to be ancillary data from other sensors, and the search limits are determined by typical sensors’ errors: $S\hat{S}\hat{T}_{\text{ancillary}} - 0.3^\circ\text{C} \leq \hat{S}\hat{S}\hat{T} \leq S\hat{S}\hat{T}_{\text{ancillary}} + 0.3^\circ\text{C}$ and $U_{10 \text{ ancillary}} - 2.5 \text{ m/s} \leq \hat{U}_{10} \leq U_{10 \text{ ancillary}} +$

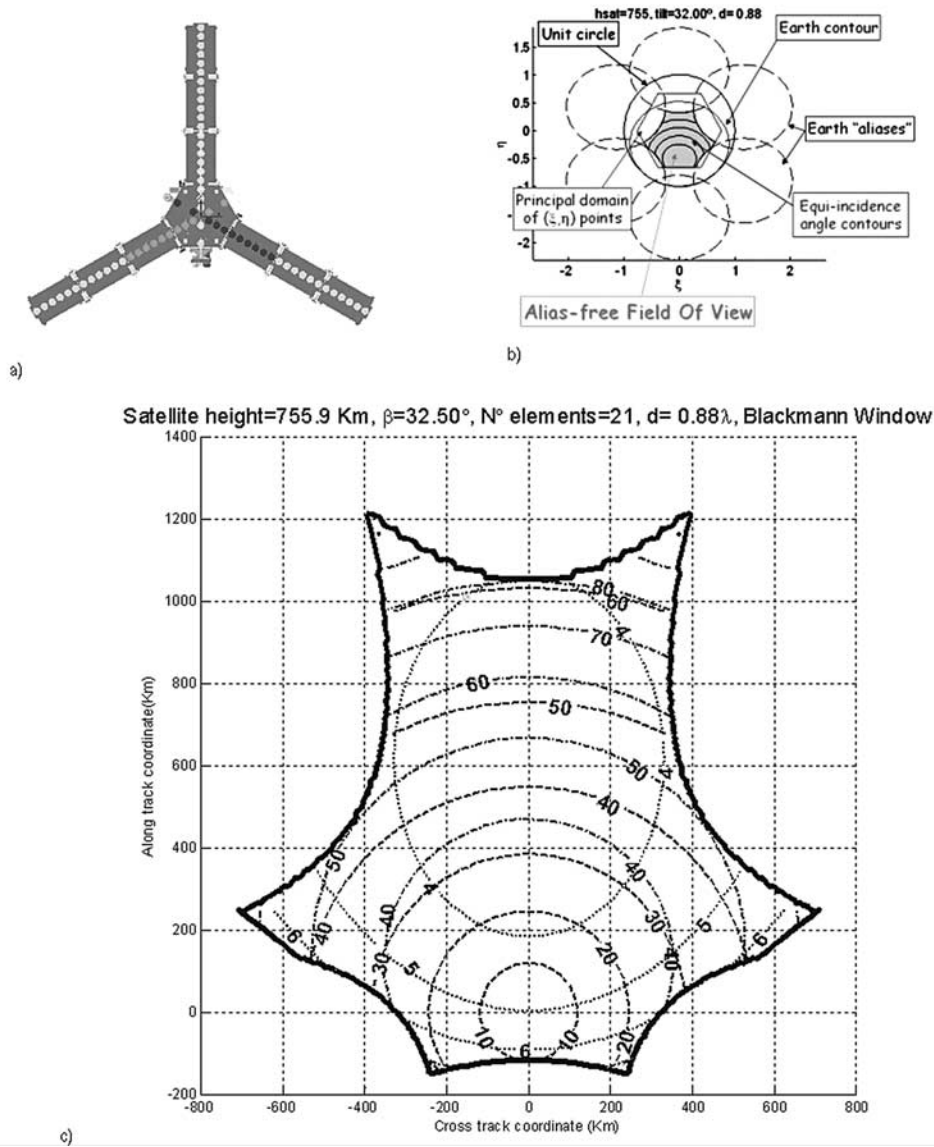


Figure 1. (a) SMOS payload module phase B configuration (courtesy of EADS-CASA Espacio, Spain). (b) SMOS observation geometry. Half-space is mapped into the unit circle in (ξ, η) coordinates. The alias-free field of view (FOV) that is imaged by the instrument is marked in light gray is enlarged up to the Earth “aliases” limit by taking into account the sky contribution. (c) Incidence angle (dashed lines from 10° to 60°, circles centered at (0, 0)); spatial resolution (dash-dot lines from 40 to 80 km, best spatial resolution 32 km); and radiometric sensitivity (dotted lines from 4 to 6 K, best radiometric sensitivity ~ 2.4 K if all available redundancies used and ~ 3.6 K if not).

2.5 m/s. In the case of sea surface salinity, no a priori information has been used except the minimum and maximum values found in the oceans and open seas: $28 \text{ psu} \leq \text{SSS} \leq 40 \text{ psu}$.

[7] The proposed approach has the following advantages [Camps et al., 2003a]: (1) avoids the singularities in the transformation from the antenna (T_x, T_y) to the Earth (T_h, T_v) reference frames [Waldteufel and Caudal,

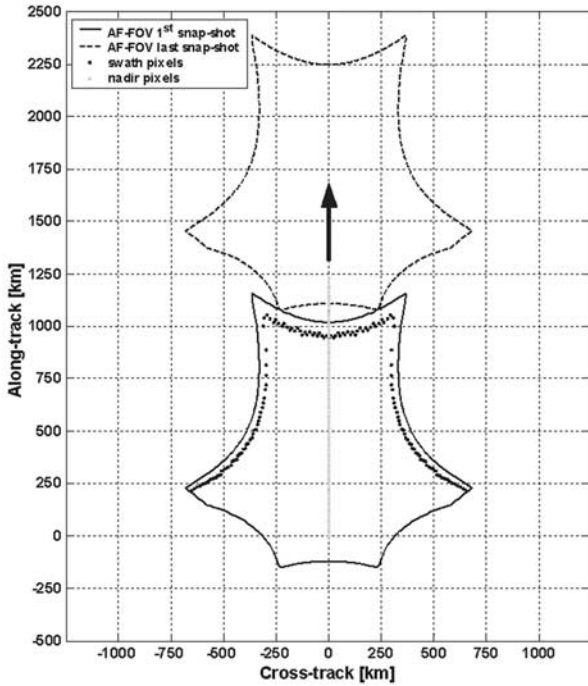


Figure 2. Evolution of nadir pixels in along-track/cross-track coordinates (gray dots at cross track = 0 km). Hexagonal-like contours indicate the position of the first (solid line) and last (dashed line) alias-free fields of views. Black dots, pixels under study covering the whole swath up to the guard pixels the first time they are seen in an overpass.

2002] since $I^{\text{measured}} = T_x + T_y = T_h + T_v$; (2) avoids the Faraday rotation correction; (3) minimizes the angular dependence of the difference between the emissivities computed with different dielectric constant models (e.g., *Klein and Swift* [1977] or *Ellison et al.* [1998]; see *Camps et al.* [2003a, Figure 4]); and (4) minimizes the emissivity angular dependence induced by other factors as the swell [*Miranda et al.*, 2003] (not accounted for in equation (1) but found in actual measurements).

[8] This study is organized as follows. Section 2 explains the atmospheric and sky radiometric corrections that have to be applied. Section 3 details the origin of different sources of bias in the brightness temperature images and explains an external calibration technique devised to compensate them and get useful SSS estimates. Section 4 presents a complete set of simulation results of the techniques presented using the SEPS with high spatial (geophysical data maps at 1/16 of degree) and temporal resolution (daily variation) covering a whole period of 30 days. These

results are used to analyze the improvement factor by spatial and temporal averaging. Finally, section 5 summarizes the main results: the conditions for proper operation of the proposed external calibration, and the error reduction expected by spatiotemporal averaging.

2. Radiometric Correction of Brightness Temperature Images on Top of the Atmosphere

[9] The brightness temperature models in the SMOS end-to-end performance simulator include many geophysical parameters from the atmosphere, the sea, the land and the ionosphere [*Camps et al.*, 1997c; *Corbella et al.*, 2003; *Camps et al.*, 2003b]. (The geophysical parameters used in SEPS are as follows: atmospheric liquid water and rain rate; land, snow, and vegetation albedos; soil surface temperature, moisture, and roughness; vegetation height, snow depth, sea surface salinity, temperature, wind speed, and ice cover fraction; as well as the galactic noise map, the international reference ionosphere, and the international geomagnetic reference field model to model the ionosphere and the Faraday rotation.) Therefore, before applying the SSS retrieval algorithm (equation (1)) a number of radiometric corrections must be performed to derive the first Stokes parameter over the Earth's surface (I^{data} in equation (1)) from the apparent brightness temperatures measured by the instrument on top of the atmosphere ($I^{\text{measured}} = T_x + T_y$):

$$\underbrace{I^{\text{data}}}_{\substack{\text{I referred to} \\ \text{Earth's surface}}} = \underbrace{(T_x + T_y)}_{\substack{\text{I measured on} \\ \text{Top Of Atmosphere (TOA)}}} \cdot L(\theta) - \left[(\Gamma_h(\theta) + \Gamma_v(\theta)) \frac{T_{\text{SKY}}}{L(\theta)} + T_{\text{UP atm}}(\theta) L(\theta) \right] - (\Gamma_h(\theta) + \Gamma_v(\theta)) T_{\text{DN atm}}(\theta), \quad (2)$$

to account for the upwelling atmospheric noise ($T_{\text{UP atm}}$), and the downwelling atmospheric noise ($T_{\text{DN atm}}$) and the cosmic and galactic noises (T_{SKY}) that are scattered over the Earth's surface. In equation (2) $L = L_{\text{atm}} + L_{\text{ion}} \approx L_{\text{atm}} (>1)$ is the total attenuation (atmosphere + ionosphere) and $\Gamma_{h,v}(\theta)$ is the effective reflectivity of the sea surface at horizontal or vertical polarizations, and θ is the incidence angle. The effective reflectivity of the sea surface is computed as $\Gamma_{h,v}(\theta) = 1 - e_{h,v}(\theta)$, where $e_{h,v}(\theta)$ is an estimate of the sea surface's emissivity

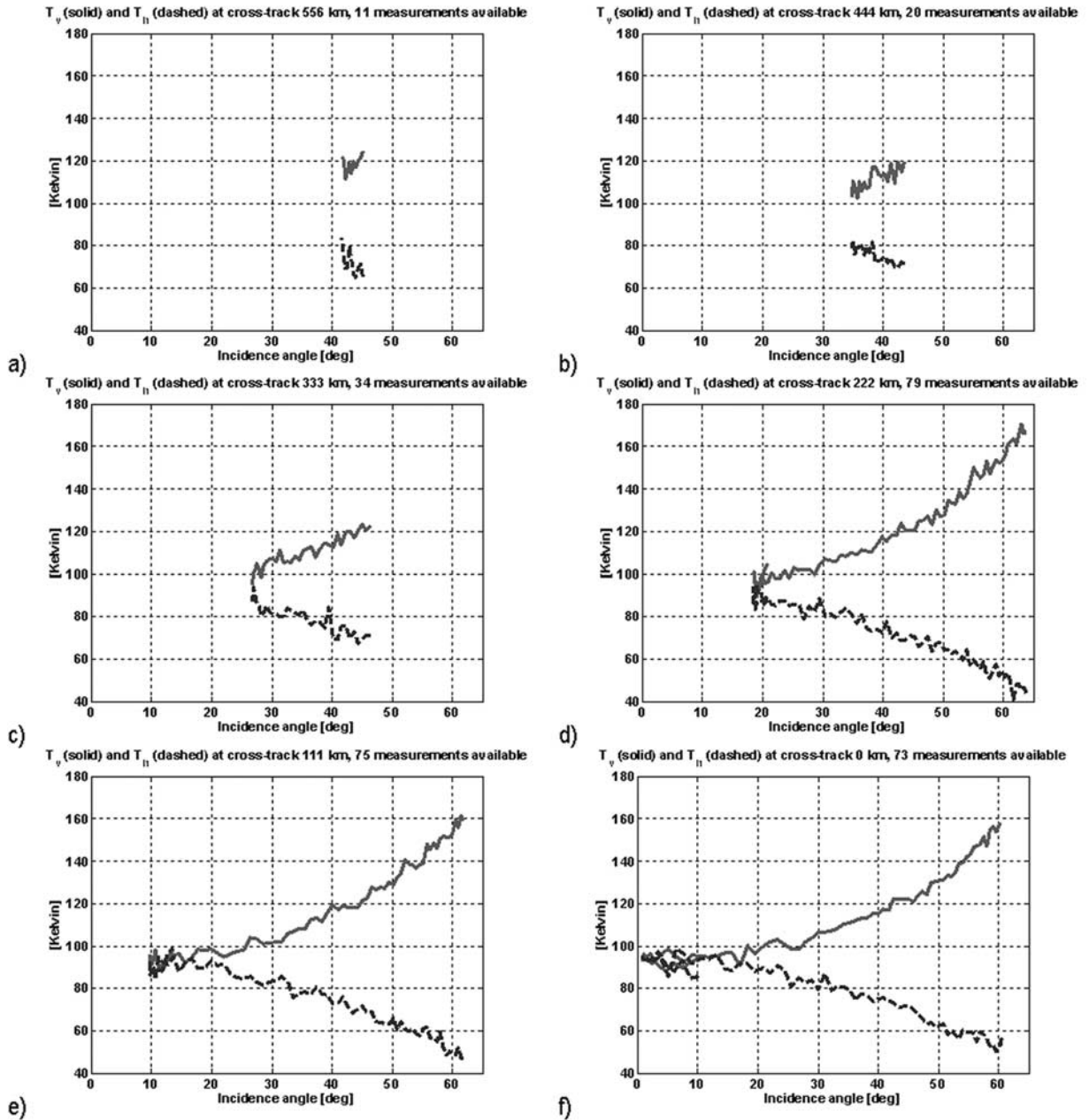


Figure 3. Series of brightness temperature observations over the Earth for different cross-track distances to the satellite’s ground track. Owing to the shape of the alias-free FOV (light gray in Figure 1b), the number of observations increases as the dwell line approaches the ground track, reaching a maximum around the cross-track position 250 km, and then slightly decreases again. Each observation is acquired at a different incidence angle. Pixels in dwell lines close to the ground track are imaged twice at some incidence angles, in the fore and aft directions, as it is clearly seen in Figure 3f.

(equation (3)), which is computed from $\Gamma_{h,v}^{specular}$, the square of the module of the Fresnel reflection coefficient, and the ancillary data:

$$e_h \approx \left(1 - \Gamma_h^{specular}(SST_{ancillary}, SSS_{ancillary}, \theta) \right) + 0.2 \left(1 + \frac{\theta}{55^\circ} \right) \frac{U_{10_{ancillary}}}{SST_{ancillary}}, \quad (3a)$$

$$e_v \approx \left(1 - \Gamma_v^{specular}(SST_{ancillary}, SSS_{ancillary}, \theta) \right) + 0.2 \left(1 - \frac{\theta}{55^\circ} \right) \frac{U_{10_{ancillary}}}{SST_{ancillary}}. \quad (3b)$$

Ancillary data used in the simulations are as follows: sea surface temperature ($SST_{ancillary}$), sea surface salinity ($SSS_{ancillary}$), and wind speed ($U_{10_{ancillary}}$). Sea state is modeled by a simple linear fit to Hollinger's data [Hollinger, 1971] with U_{10} as parameter. Other effects are neglected. More recent measurements [Camps et al., 2003a, 2004a] have found new values for the wind-dependent terms in equations (3a) and (3b). Within the measurements error bars, these values can be fitted by a linear expressions as in equations (3a) and (3b), with slightly different parameters. In the present study the correction terms in equation (2) are assumed to be at zenith equal to: $T_{UP_{atm}} \approx 1.86$ K, $T_{DN_{atm}} \approx 2.10$ K [Goodberlet and Miller, 1997], and $L \approx L_{atm} \approx 0.0402$ dB. Off-zenith, to account for the actual atmospheric path due to Earth's curvature, these values are divided by the cosine of an equivalent incidence angle:

$$\cos \theta_{eq} = \frac{h_{atm}}{\sqrt{R_T^2 \cos^2(\theta) + (h_{atm} + 2R_T)h_{atm}} - R_T \cos(\theta)}, \quad (4)$$

where h_{atm} is the atmosphere height, and R_T is the Earth's radius.

[10] Last, the sky (cosmic+galactic) noise in equation (2) is estimated from satellite's position, attitude, time, and the 1420 MHz sky map [Reich, 1982; Reich and Reich, 1986] (see also <http://skyview.gsfc.nasa.gov/>) as described in the work of LeVine and Abraham [2004].

[11] It should be pointed out that in this simplified model: (1) the azimuthal signature of e_h and e_v has been neglected since to date no field experiments have provided an evidence of it within the measurement accuracy (± 0.1 K), except in very particular cases [Camps et al., 2004a]; (2) equations (3a) and (3b) represent the first-order Taylor's expansion of $e_h(U_{10})$ and $e_v(U_{10})$, which is very accurate at L band for wind speeds in the range 2–18 m/s [Etcheto et al., 2004, Figure 8]; and (3) in the scattered terms ($\Gamma_h(\theta) + \Gamma_v(\theta)T_{SKY}/L(\theta)$ and ($\Gamma_h(\theta) +$

$\Gamma_v(\theta)T_{DN_{atm}}(\theta)$ only the specular reflection terms are considered.

3. External Calibration of the Brightness Temperature Images

[12] The properties of the brightness temperature images obtained from SEPS exhibit an excellent agreement with the SMOS error budget predictions in terms of radiometric accuracy and sensitivity [Camps et al., 2003c]. However, when comparing these images with respect to the ideal ones (same angular resolution but without noise and instrumental errors), there is often a bias. Three sources of bias have been identified:

[13] 1. Instrumental inaccuracies in the noise injection radiometers (NIRs) used to measure the antenna temperature (average value of the scene). These errors are: thermal noise ($\Delta T \sim 0.2$ K), offset, and linearity errors. While the offset causes a scene-independent brightness temperature bias, the linearity error causes a brightness temperature error, which is dependent on the antenna temperature corresponding to the scene being imaged. These terms are also temperature-dependent and therefore depend on satellite's argument of the latitude.

[14] 2. Inherent difference between the antenna temperature (average value of the brightness temperature of the scene in the unit circle) and the average brightness temperature in the AF-FOV (Figure 1b) since the AF-FOV does not cover the whole space. This error has been found to be more important in inhomogeneous scenes (e.g., near the coastline).

[15] 3. Sun contribution to the antenna temperature. Even though some image reconstruction algorithms include Sun brightness temperature estimators and cancellators such as Camps et al. [2004b], Sun cancellation is never perfect and there is always a residual error which appears as ripples ("tails" of the quasi-impulse response) and a residual contribution to the antenna temperature.

[16] If the sensitivity of the brightness temperature at nadir to the sea surface salinity is $\Delta T/\Delta SSS \approx 0.5$ K/psu at 25°C (even smaller at lower temperatures) and the goal is to achieve an SSS error of 0.1 psu, the absolute accuracy of a real aperture radiometer should be 0.05 K, which is very challenging for any type of radiometer. This level of accuracy is very unlikely in a MIRAS-type of instrument with internal calibration only [Torres et al., 1996; Corbella et al., 1998], and therefore some sort of external calibration must be envisaged.

[17] The use of one or several tie points to match the retrieved brightness temperature does not produce satisfactory results since the radiometric sensitivity of MIRAS is ~ 2.4 K at boresight, and worsens away from this direction [Camps et al., 2004c]. The proposed external calibration technique relies on the use of ancil-

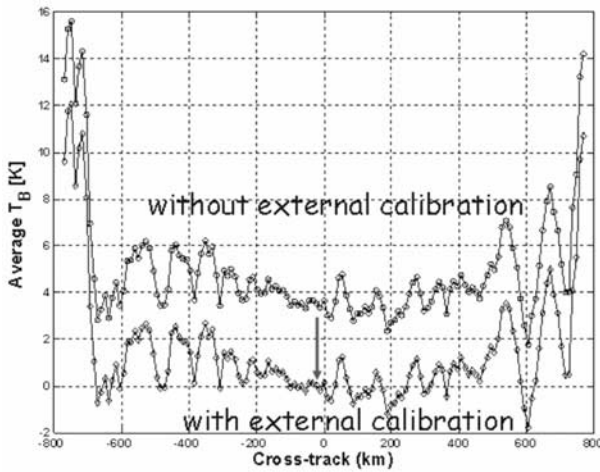


Figure 4. Brightness temperature error versus cross-track position with (diamonds) and without (circles) external calibration. Brightness temperature biases are significantly reduced by means of external calibration.

lary SST and U_{10} data, and SSS estimates to predict the brightness temperature of nadir pixels (0° incidence angle, gray dots in Figure 2), for all the snapshot images containing the pixels where the SSS is going to be retrieved (pixels marked as black dots the first time they are seen in an overpass, Figure 2). For the whole series of snapshots, the nadir brightness temperatures at both polarizations are added together to form the estimated first Stokes parameter at nadir (\hat{I}_n), and finally, the \hat{I}_n values corresponding to each snapshot are then averaged to reduce its noise (Figure 2):

$$\bar{I} = \frac{1}{N_{\text{observations}}} \sum_{n=1}^{N_{\text{observations}}} \hat{I}_n = \frac{1}{N_{\text{observations}}} \sum_{n=1}^{N_{\text{observations}}} \left(T_{\text{Bh}}^{\text{model}} \left(\theta = 0^\circ, \text{SST}_{\text{ancillary}}, \text{SSS}_{\text{ancillary}}, U_{10 \text{ ancillary}} \right)_n + T_{\text{Bv}}^{\text{model}} \left(\theta = 0^\circ, \text{SST}_{\text{ancillary}}, \text{SSS}_{\text{ancillary}}, U_{10 \text{ ancillary}} \right)_n \right) \quad (5)$$

The same procedure is followed with the measured data. Finally, the average bias for the set of snapshots used in the retrieval is computed as

$$\Delta I = \bar{I}^{\text{data}} - \bar{I}, \quad (6)$$

which is then subtracted from I_n^{data} , for all image pixels in equation (1), and for all the snapshots in which the pixel is visible.

[18] The performance of this technique improves with: (1) the number of visible snapshots ($N_{\text{observations}}$) with nadir pixels corresponding to sea, and (2) homogeneous brightness temperature scenes (smaller antenna temperature bias value from second source), which is the case of the ocean. (Nadir land pixels are not considered since their brightness temperature depends on more geophysical parameters and exhibit a much larger variability than in the case of sea.)

[19] Figure 4 shows an example of application of the external calibration to a homogeneous scene in the equatorial Pacific (scenario 3, section 4) corresponding to 4 February 2003. To apply the external calibration technique, a total of 79 snapshots were simulated for each overpass (covering the longest dwell line) every 2.4 s over 3 min. (In SMOS, there is only one receiver per antenna, and the antenna polarization switch has to be commuted: a whole brightness temperature image is obtained every 2.4 s in both operation modes, dual polarization and full polarimetric [Martín-Neira et al., 2002].) The only overpasses that are valid and have been considered in this study correspond to ascending orbits (to avoid diurnal SST variations), with at least part of the satellite's ground track over the sea (feasible external calibration since ground track pixels correspond to the sea), and with the buoy pixel inside the swath edges (center part of Figure 4) in order to have correct SSS retrieved values. As it is clearly seen in Figure 4, the average error of the brightness temperature versus the cross-track position with external calibration is significantly reduced. Figure 5 shows the retrieved SSS with and without external calibration for bias compensation. If the external calibration is not applied, retrieved SSS biases are significant (~ -5.5 psu), while when the external calibration is applied the SSS error is smaller than ± 1 psu in a swath width of approximately ± 700 km.

4. Simulation Results

[20] In the work of Camps et al. [2003a] a SSS retrieval study was performed for the SMOS instrument estimating the performances that can be expected from a single overpass over different scenarios with constant SSS, SST, and U_{10} . For an ideal system only limited by thermal noise, the SSS retrieval error in one overpass is ~ 1 psu. To try to reduce this error down to 0.1 psu, SSS retrievals can be averaged both in time up to 10 or 30 days and in space up to 200 km [Smith and Lefèvre, 1997].

[21] In the work of Camps et al. [2002] the reduction of the SSS retrieval error by temporal averaging was studied using NDBC data (see <http://www.ndbc.noaa.gov/>) for three fixed representative locations (Table 2) during a whole month of January. Simulation results showed that averaging during 30 days, the SSS retrieval

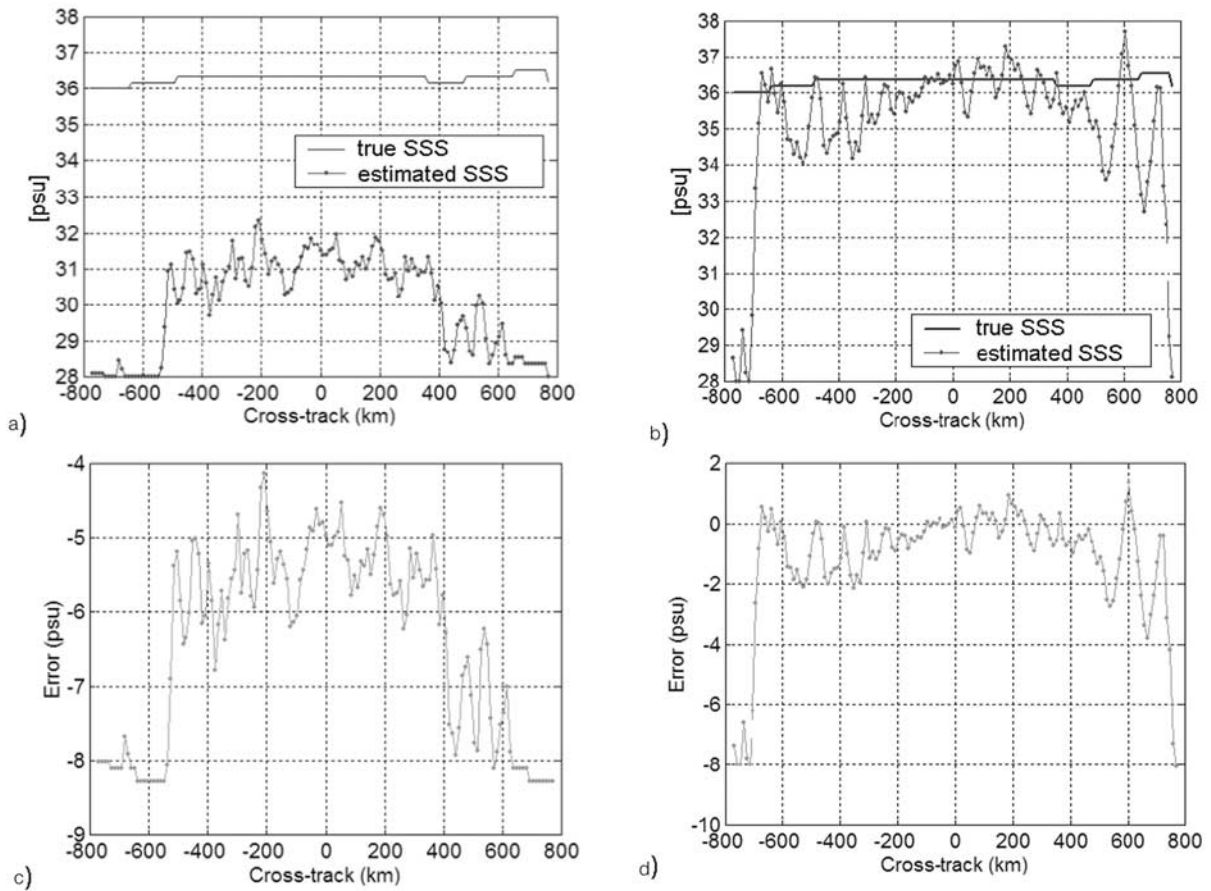


Figure 5. (a and b) Sea surface salinity retrieval without and (c and d) with external calibration, retrieved sea surface salinity (Figures 5a and 5b), and sea surface salinity error (Figures 5c and 5d).

error ranged from 0.12 psu to 1.06 psu, depending on the scenario location and the meteorological/oceanographic conditions. The impact of geophysical modeling errors and biases in the first Stokes parameter were also

analyzed, indicating a maximum allowable bias of $|I_{\text{bias}}| < 0.22$ K to achieve the 0.1 psu goal.

[22] In this study the SSS error reduction by spatial averaging is analyzed at four different levels: SMOS

Table 2. Number of Satellite Overpasses for Each Scenario^a

Scenario	Reference Buoy	Location	Descending Orbits	Ground Track Pixels = Land	Location at Swath Edge	Valid Overpasses
1	station 46184, North Nomad	53.91°N, 138.85°W (coast of Alaska)	51	9	4	39
2	station 41025, Diamond Shoals	35.15°N, 75.29°W (coast of North Carolina)	27	4	2	14
3	station 51028, Christmas Island DWA	0.00°N, 153.88°W (equatorial Pacific)	28	0	4	24

^aThe present study has only considered overpasses in ascending orbits, with valid external calibration (external calibration pixels = ocean pixels), and with the reference SMOS pixel outside the swath edges to provide correct SSS retrieved values.

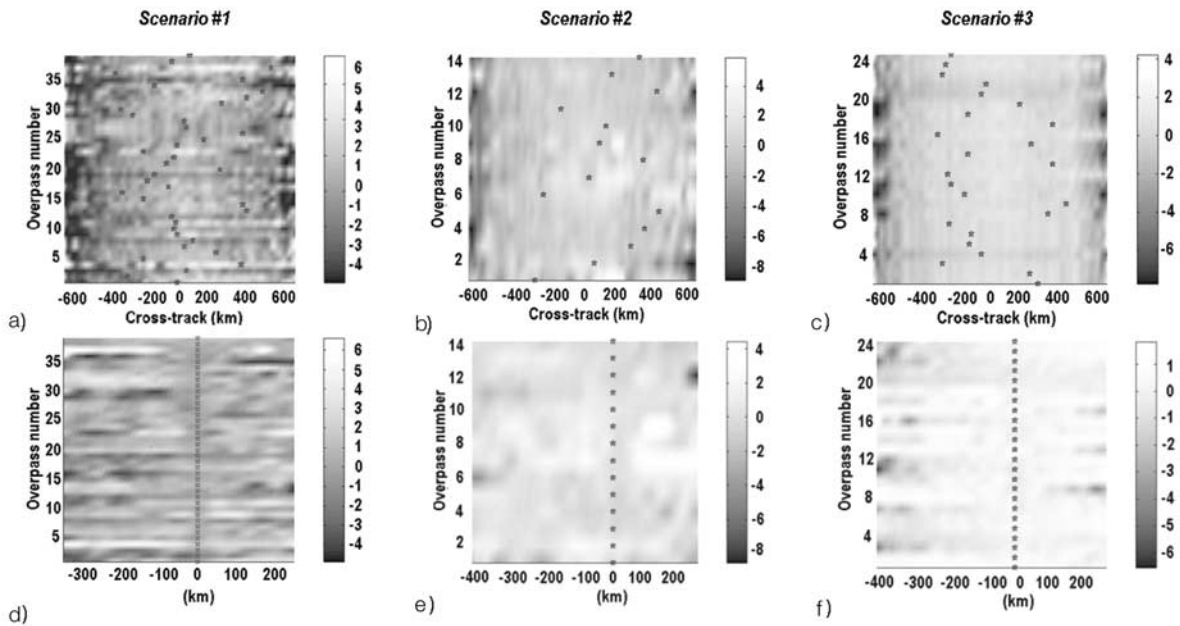


Figure 6. (a–c) Gray level indicates sea surface salinity retrieval error (psu) as a function of the valid satellite overpass and the cross-track coordinate. Scenario positions in the cross-track are indicated by stars. (d–f) Spatial averaging requires the alignment of different overpasses so that all cross-track coordinates are referred to the same geographical locations (kilometers referred to pixel under study).

pixel size (≥ 30 km, varying with pixel location in the AF-FOV), 50 km, 100 km, and 200 km. The error reduction by temporal averaging is then also studied in periods of 10 or 30 days. The global data used in SEPS [Meeson *et al.*, 1995] are at $1^\circ \times 1^\circ$ resolution, which corresponds to ~ 110 km at the equator, larger than the SMOS spatial resolution. Therefore, in order to be able to study the improvement by spatial averaging, SSS, SST, and U_{10} input data is needed for the SEPS brightness temperature generator at a spatial resolution higher than the best SMOS spatial resolution [Camps *et al.*, 2003b]. The SST and U_{10} input data were provided by the Naval Research Laboratory (NRL) as outputs of the layered ocean model (see http://www7320.nrlssc.navy.mil/global_nlom/) at a spatial resolution of $1^\circ/16$ and a daily variation covering a whole period of 30 days from 14 January to 13 February 2003. The only SSS data available were the original Levitus data at 1° resolution. However, taking into account that the SMOS revisit time is 3 days at the equator, small-scale (~ 7 km at the equator) and temporal (1 day) variabilities are retained since they are mostly induced by the wind fields. Only at high latitudes, the temporal variability is lost (revisit time < 1 day), but some randomness is kept owing to instru-

mental noise and the changing position of the pixel under observation in the swath.

[23] The average values of the SSS, SST, and U_{10} for the period under study in the reference scenarios are: (1) scenario 1, SSS = 32.797 psu, SST = 6.83°C , and $U_{10} = 6.60$ m/s; (2) scenario 2, SSS = 36.551 psu, SST = 22.54°C , and $U_{10} = 8.41$ m/s; and (3) scenario 3, SSS = 35.402 psu, SST = 25.54°C , and $U_{10} = 3.85$ m/s.

[24] End-to-end simulations have been performed using the phase B SMOS configuration (Figure 1a), with 2.4 s between consecutive snapshots (1.2 s per polarization in dual-polarization mode) during the 3 min overpass. (An end-to-end simulation means the modeling of the whole process from geophysical parameters to brightness temperatures at the antenna reference frame, to raw visibility samples (including all instrumental errors), to error-corrected visibility samples, to reconstructed brightness temperatures in the antenna (or Earth) reference frame, and to retrieved geophysical parameters [Camps *et al.*, 2003b].) Table 2 summarizes the total number of descending orbits; the number of descending orbits in which the ground track is over land and therefore cannot be used for external calibration; the number of descending orbits in which the scenario

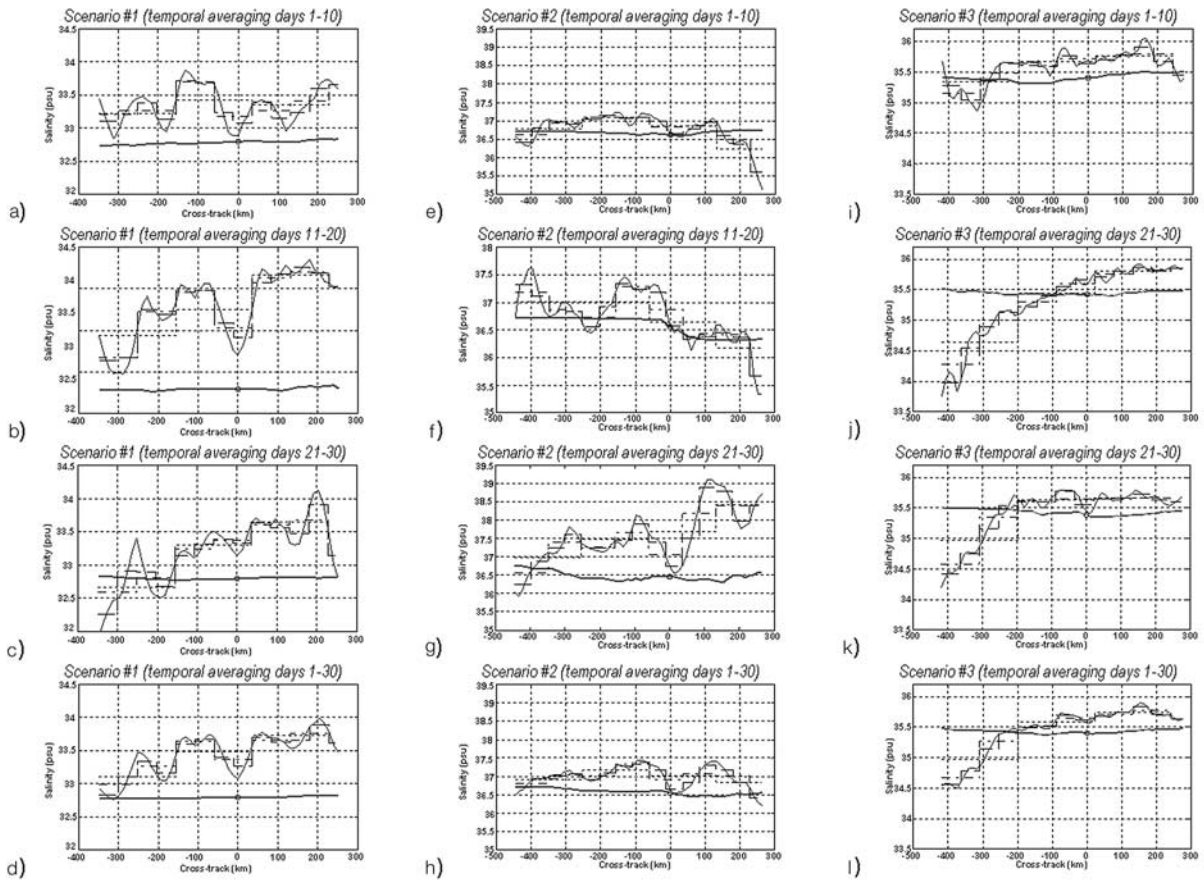


Figure 7. Sea surface salinity (SSS) retrieval for buoy numbers (a–d) 1, (e–h) 2, and (i–l) 3 in blocks of 10 days (Figures 7a, 7e, and 7i, days 1–10; Figures 7b, 7f, and 7j, days 11–20; Figures 7c, 7g, and 7k, days 21–30) and 30 days (Figures 7d, 7h, and 7l) for different levels of spatial averaging (circles at cross track = 0 km, average value at buoy position; thick black line, time average of actual SSS values; gray line, time average retrieved SSS values; thin black solid line, time average retrieved SSS values averaged in blocks of 50 km; black dashed line: time average retrieved SSS values averaged in blocks of 100 km; black dotted line, time average retrieved SSS values averaged in blocks of 200 km).

appears in the edge of the swath and the retrievals are too noisy; and finally, the number of remaining descending orbits that are valid.

[25] As shown in the work of Camps *et al.* [2002, 2003a], the SSS retrieval RMS error in one overpass is on the order of 1 psu. To reduce this error down to 0.1 psu, SSS retrievals can be averaged both in time up to 10 or 30 days, and in space up to 200 km [Smith and Lefèbvre, 1997]. For proper intercomparison, the average retrieved SSS values are compared with the average original SSS values. The SSS retrievals at location of scenario 3 are better than the rest for two reasons: (1) the water is warmer and the average wind speed is small, and (2) the buoy is farther away from the coast than

swath, and nadir pixels in all overpasses can be used in the external calibration. This is not the case of scenarios 1 and 2, which are very close to the coast.

[26] Figure 6 shows the sea surface salinity retrieval error as a function of the cross-track coordinate for all valid overpasses (Table 2). As expected, the SSS retrieval error is larger at swath edges due to the smaller number of observations ($N_{\text{observations}}$), the smaller angular variation, and the higher noise, and it is larger for scenario 1 than for scenarios 2 and 3 owing to the cooler sea. Figure 7 shows the sea surface salinity retrieval for the three buoys in blocks of 10 days (days 1–10, days 11–20, and days 21–30) and 30 days, at different levels of spatial averaging (at buoy position, in blocks of 50,

Table 3. SSS Retrieval Errors for Different Time and Spatial Averaging Levels

	Scenario	Temporal Averaging, days	Spatial Averaging			
			$\Delta\text{SSS}_{\text{SMOS pixel, psu}}$	$\Delta\text{SSS}_{50 \text{ km, psu}}$	$\Delta\text{SSS}_{100 \text{ km, psu}}$	$\Delta\text{SSS}_{200 \text{ km, psu}}$
Figure 7a	1	1–10	0.089	0.280	0.392	0.647
Figure 7b		11–20	0.414	0.614	0.731	0.948
Figure 7c		21–30	0.350	0.528	0.575	0.505
Figure 7d	2	1–30	0.284	0.474	0.566	0.700
Figure 7e		1–10	0.040	0.019	0.184	0.205
Figure 7f		11–20	0.009	0.061	0.289	0.167
Figure 7g	3	21–30	0.284	0.293	0.619	1.259
Figure 7h		1–30	0.099	0.112	0.346	0.493
Figure 7i		1–10	0.286	0.244	0.324	0.307
Figure 7j	3	11–20	0.161	0.240	0.176	0.026
Figure 7k		21–30	0.061	0.157	0.246	0.206
Figure 7l		1–30	0.169	0.214	0.249	0.180

100, and 200 km). Numerical results are provided in Table 3.

[27] A close look to Figures 6b and 6c shows that the SSS retrieval error is correlated with the cross-track coordinate (vertical strips), indicating that antenna pattern errors are not fully corrected by the image reconstruction algorithms and translate into the brightness temperature images. (Receiver errors are uncorrelated from overpass to overpass since the intercalibration period is smaller than the revisit time.) In principle, it would be expected that averaging different SSS retrievals would reduce the SSS error since the SSS retrievals at the scenarios' positions appear in different swath positions at each overpass (stars in Figure 6 indicate the buoy position of the pixel under study), and the error correlation with the cross-track position is lost. However, the examination of Table 3 shows that, for a given buoy and time period, it is 10 or 30 days and spatial averaging does not produce an improvement of the error (except in Figure 7j), although it does reduce the spatial oscillations of the error (see Figure 7).

[28] In the ideal case, if N statistically independent measurements have an error with a zero-mean Gaussian distribution and standard deviation equal to σ , the standard deviation of their average is σ/\sqrt{N} . That is, the error is reduced by a $1/\sqrt{N}$ factor. The question now is to understand the error reduction factor that can be expected from temporal averaging of SSS retrievals at different spatial resolution levels: at SMOS pixel size, at 50 km, at 100 km, and at 200 km. In order to make an homogeneous comparison with the ideal case, the error reduction factor is computed taking as the first measurement the one with the largest error and normalizing the resulting standard deviation of the error of the SSS average with respect to it.

[29] Figures 8a, 8b, and 8c show the computed error reduction factor for the three scenarios under study. In all three cases and for all levels of spatial averaging:

(1) when the number of overpasses that are averaged is large, the error reduction factor tends to $1/\sqrt{N}$ (black solid line with dots), which means that the measurements acquired (or simulated) at different times are uncorrelated; (2) the error reduction factor is best when the temporal average is performed directly at SMOS pixel level (no spatial averaging); and (3) the error reduction factor (for the same number of overpasses averaged) is larger when the variability is larger (scenario 1, cooler sea and scenario 2, largest wind speed). The same performance is obtained if the spatial averaging is performed after the temporal averaging.

5. Conclusions

[30] This study has completed previous SMOS-oriented SSS retrieval studies [Camps *et al.*, 2002, 2003a] analyzing the reduction of the SSS retrieval error that can be expected from temporal and spatial averaging. In order to achieve salinity retrievals with the required accuracy for oceanographic applications, an external calibration technique has been devised to compensate the biases that appear in brightness temperature images obtained by 2-D synthetic aperture radiometers.

[31] We found the following.

[32] 1. SSS retrieval errors are correlated with the cross-track position, indicating the presence of residual antenna patterns in the brightness temperature images.

[33] 2. In general, spatial averaging does not reduce the SSS retrieval error as expected. This is probably due to the intrapixel variability in one side, and on the other side, to the spatial correlation of geophysical parameters and the partial correlation of residual radiometric errors in the cross-track direction, which reduces the effectiveness of spatial averaging.

[34] 3. Temporal averaging reduces the error approximately as the inverse of the square root of the number of

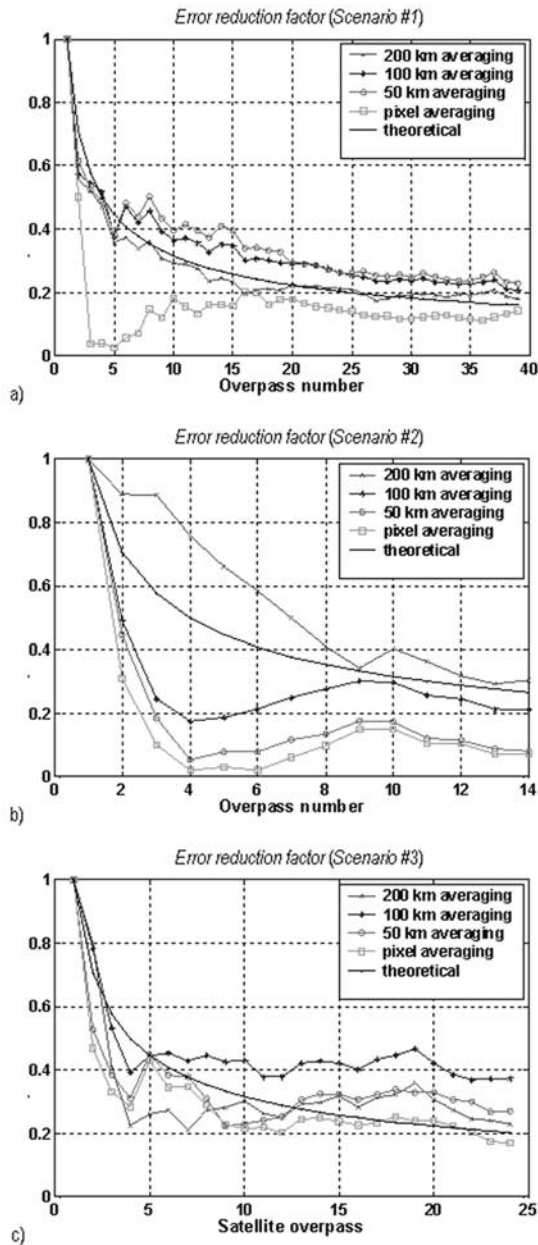


Figure 8. Averaging improvement factor at different spatial resolution levels and theoretical improvement ($1/\sqrt{N}$) for scenarios: (a) 1, (b) 2, and (c) 3.

measurements being averaged (noise in brightness temperature measurements is independent from overpass to overpass and the pixel position in the cross track varies from snapshot to snapshot). The error reduction is slightly higher for large retrieval errors and slightly lower for small retrieval errors (homogeneous scenes).

[35] The SSS retrieval accuracy at 30 days temporal resolution and 200 km spatial resolution for a SMOS-like instrument including thermal noise, all instrumental errors, error correction, image reconstruction, and radiometric corrections for atmospheric and sky noises, is expected to be ~ 0.7 psu for a cold sea (scenario 1), ~ 0.5 psu for a medium latitude sea (scenario 2), and ~ 0.2 psu for a tropical sea (scenario 3). These quotes may be improved if the descending orbits are processed including corrections for diurnal SST variations, and if the external calibration technique proposed is extended to off-nadir pixels, and eventually to all sea pixels, which would require an accurate modeling of the seawater emissivity versus incidence angle and mainly sea state. This modification of the external calibration can significantly improve the performance for locations close to the coast (case of scenarios 1 and 2).

[36] **Acknowledgments.** This work has been supported by the Spanish Government under grants MCYT and EU FEDER TIC2002-04451-C02-01 and PNE-009/2001-C-02. The authors are very grateful to Jerry L. Miller, Associate Director for Ocean, Atmosphere, and Space Research Office of Naval Research-Global (ONRG), for providing the sea surface temperature and wind speed outputs from the Naval Research Laboratory (NRL) Layered Ocean Model (NLOM) used in these simulations. The authors would also like to thank three anonymous reviewers for their comments to improve the clarity of this work.

References

- Camps, A., J. Bará, I. Corbella, and F. Torres (1997a), The processing of hexagonally sampled signals with standard rectangular techniques: Application to 2D large aperture synthesis interferometric radiometers, *IEEE Trans. Geosci. Remote Sens.*, 35, 183–190.
- Camps, A., J. Bará, F. Torres, I. Corbella, and J. Romeu (1997b), Impact of antenna errors on the radiometric accuracy of large aperture synthesis radiometers: Study Applied to MIRAS, *Radio Sci.*, 32(2), 657–668.
- Camps, A., F. Torres, J. Bará, I. Corbella, M. Pino, and M. Martín Neira (1997c), Evaluation of MIRAS spaceborne instrument performance: Snap shot radiometric accuracy and its improvement by means of pixel averaging, *Proc. SPIE*, 3221, 43–52.
- Camps, A., J. Bará, F. Torres, and I. Corbella (1998a), Extension of the CLEAN technique to the microwave imaging of continuous thermal sources by means of aperture synthesis radiometers, *Progr. Electromagn. Res.*, 18, 67–83.
- Camps, A., F. Torres, I. Corbella, J. Bará, and P. de Paco (1998b), Mutual coupling effects on antenna radiation pattern: An experimental study applied to interferometric radiometers, *Radio Sci.*, 33(6), 1543–1552.
- Camps, A., N. Duffo, M. Vall-Ilossera, and B. Vallespin (2002), Sea surface salinity retrieval using multi-angular L-band

- radiometry: Numerical study using the SMOS end-to-end performance simulator, paper presented at IGARSS 2002, Inst. of Electr. and Electron. Eng., Toronto, Ont., Canada.
- Camps, A., et al. (2003a), L-band sea surface emissivity: Preliminary results of the WISE-2000 campaign and its application to salinity retrieval in the SMOS mission, *Radio Sci.*, 38(4), 8071, doi:10.1029/2002RS002629.
- Camps, A., I. Corbella, M. Vall-llossera, N. Duffo, F. Marcos, F. Martínez-Fadrique, and M. Greiner (2003b), The SMOS end-to-end performance simulator: Description and scientific applications, paper presented at International Geoscience and Remote Sensing Symposium, Toulouse, France.
- Camps, A., I. Corbella, F. Torres, N. Duffo, and M. Vall-llossera (2003c), SMOS system performance model and error budget, *Rep. SO-TN-UPC-PLM-02*, Eur. Space Res. and Technol. Cent., Noordwijk, Netherlands.
- Camps, A., et al. (2004a), The WISE 2000 and 2001 campaigns in support of the SMOS Mission: Sea surface L-band brightness temperature observations and their application to multi-angular salinity retrieval, *IEEE Trans. Geosci. Remote Sens.*, 42(4), 804–823.
- Camps, A., M. Vall-llossera, N. Duffo, M. Zapata, I. Corbella, F. Torres, and V. Barrena (2004b), Sun effects in 2D aperture synthesis radiometry imaging and their cancellation, *IEEE Geosci. Remote Sens.*, 42(6), 1161–1167.
- Camps, A., M. Zapata, I. Corbella, F. Torres, M. Vall-llossera, N. Duffo, C. García, and F. Martín (2004c), SMOS radiometric performance evaluation using SEPS: Evaluation of thermal drifts, paper presented at International Geoscience and Remote Sensing Symposium IGARSS 2004, Inst. of Electr. and Electron. Eng., Anchorage, Alaska.
- Corbella, I., F. Torres, A. Camps, and J. Bará (1998), A new calibration technique for interferometric radiometers, *Proc. SPIE*, 3498, 359–366.
- Corbella, I., A. Camps, M. Zapata, F. Marcos, F. Martínez, F. Torres, M. Vall-llossera, N. Duffo, and J. Bará (2003), End-to-end simulator of two-dimensional interferometric radiometry, *Radio Sci.*, 38(3), 8058, doi:10.1029/2002RS002665.
- Ellison, W., A. Balana, G. Delbos, K. Lamkaouchi, L. Eymard, C. Guillou, and C. Prigent (1998), New permittivity measurements of sea water, *Radio Sci.*, 33(3), 639–648.
- Etcheto, J., E. Dinnat, J. Boutin, A. Camps, J. Miller, S. Contardo, J. Wesson, J. Font, and D. Long (2004), Wind speed effect on L-band brightness temperature inferred from EuroSTARRS and WISE 2001 field experiments, *IEEE Trans. Geosci. Remote Sens.*, 42(10), 2206–2213.
- Gabarró, C., M. Vall-llossera, J. Font, and A. Camps (2003), Determination of sea surface salinity and wind speed by L-band microwave radiometry from a fixed platform, *Int. J. Remote Sens.*, 24, 1–18.
- Goodberlet, M., and J. Miller (1997), NPOESS-sea surface salinity: Final report, *NOAA contract 43AANE704017*, Silver Spring, Md.
- Hollinger, J. P. (1971), Passive microwave measurements of sea surface roughness, *IEEE Trans. Geosci. Electron.*, 9(3), 165–169.
- Klein, L. A., and C. T. Swift (1977), An improved model for the dielectric constant of sea water at microwave frequencies, *IEEE J. Ocean. Eng.*, 2(1), 104–111.
- LeVine, D. M., and S. Abraham (2004), Galactic noise and passive remote sensing from space at L-band, *IEEE Trans. Geosci. Remote Sens.*, 42(1), 119–129.
- Martín-Neira, M., S. Ribó, and A. J. Martín-Polegre (2002), Polarimetric mode of MIRAS, *IEEE Trans. Geosci. Remote Sens.*, 40(8), 1755–1768.
- Meeson, B. W., F. E. Corprew, J. M. P. McManus, D. M. Myers, J. W. Closs, K. J. Sun, D. J. Sunday, and P. J. Sellers (1995), *ISLSCP Initiative I—Global Data Sets for Land-Atmosphere Models, 1987–1988* [CD-ROM], vol. 1–5, NASA, Greenbelt, Md.
- Miranda, J. J., M. Vall-llossera, A. Camps, N. Duffo, I. Corbella, and J. Etcheto (2003), Sea state effect on the sea surface emissivity at L-band, *IEEE Trans. Geosci. Remote Sens.*, 41(10), 2307–2315.
- Press, W., S. Teukolsky, W. Vetterling, and B. Flannery (1992), *Numerical Recipes in C: The Art of Scientific Computing*, 2nd ed., Cambridge Univ. Press, New York.
- Reich, W. (1982), A radio continuum survey of the northern sky at 1420 MHz—Part I, *Astron. Astrophys. Suppl. Ser.*, 48, 219–297.
- Reich, P., and W. Reich (1986), A radio continuum survey of the northern sky at 1420 MHz—part II, *Astron. Astrophys. Suppl. Ser.*, 63, 205–292.
- Smith, N., and M. Lefèbvre (1997), The Global Ocean Data Assimilation Experiment (GODAE), Monitoring the oceans in the 2000s: An integrated approach, paper presented at International Symposium, Cent. Natl. d’Etudes Spatiales, Biarritz, France, 15–17 Oct.
- Thompson, A. R., J. M. Moran, and G. W. Swenson (1986), *Interferometry and Synthesis in Radio Astronomy*, John Wiley, Hoboken, N. J.
- Torres, F., A. Camps, J. Bará, I. Corbella, and R. Ferrero (1996), On-board phase and modulus calibration of large aperture synthesis radiometers: Study applied to MIRAS, *IEEE Trans. Geosci. Remote Sens.*, 34, 1000–1009.
- Torres, F., A. Camps, J. Bará, and I. Corbella (1997), Errors on the radiometric resolution of large 2D aperture synthesis radiometers: Study applied to MIRAS, *Radio Sci.*, 32(2), 629–642.
- Waldteufel, P., and G. Caudal (2002), About off-axis radiometric polarimetric measurements, *IEEE Trans. Geosci. Remote Sens.*, 40(6), 1435–1439.

L. Batres, A. Camps, I. Corbella, N. Duffo, F. Torres, and M. Vall-llossera, Department of Signal Theory and Communications, Universitat Politècnica de Catalunya, Campus Nord, D4-016, E-08034 Barcelona, Spain. (camps@tsc.upc.es)